Time Resolved High Dynamic Range PIV using Local Uncertainty Estimation Methods

Tim Persoons[1,*], Rudi O'Reilly Meehan[1], Darina B. Murray[1]

1: Department of Mechanical & Manufacturing Engineering, Parsons Building, Trinity College, Dublin, Ireland
* Correspondent author: tim.persoons@tcd.ie

Abstract The dynamic velocity range of particle image velocimetry (PIV) is determined by the ratio of maximum to minimum resolvable particle displacement. Various techniques have been developed to extend the dynamic range by increasing the maximum or reducing the minimum measurable displacement. Nevertheless flows with a wide velocity range still challenge conventional PIV methods. In this paper, a basic axisymmetric jet flow is used as a benchmark case yet similar flow conditions occur in many aerodynamic and industrial engineering applications. Using multiple pulse separation (MPS) acquisition in combination with a new criterion for the local optimal pulse separation, this paper presents a new time-resolved high dynamic range (HDR) PIV methodology. The optimality criterion is based on maximizing a heuristic vector quality metric combining the correlation peak ratio with the estimated local displacement uncertainty and magnitude, expressed as a local signal-to-noise ratio. The method is demonstrated in this paper in its simplest form, requiring no specialized pulse timing system but only a standard time-resolved double-pulsed PIV system. The vector fields evaluated from double-frame cross-correlation and those evaluated from time-series cross-correlation are combined, resulting in an increase in dynamic velocity range of 34:1 compared to conventional best practice double-frame PIV. Significant enhancements are shown in the measured turbulence intensity and estimated signal-to-noise ratio throughout the flow field, but especially in the entrainment region and the outer shear layer. Hot-wire anemometry is used in selected characteristic locations in the flow field as independent reference for the PIV measurements. The results show that time-resolved HDR method automatically selects the most optimal pulse separation in each vector location, as a function of time. The method can be further improved by incorporating alternative uncertainty estimation methods, or by using more advanced pulse timing systems. The HDR method is implemented based on readily available data; it has a low computational cost and is fully compatible with conventional multi-grid vector evaluation algorithms.

1. Introduction

1.1 Dynamic Velocity Range of PIV

The dynamic velocity range of particle image velocimetry (PIV), DR_V, is defined as the ratio of maximum to minimum resolvable velocity, or $DR_V = V_{max}/\sigma_V = s_{max}/\sigma_s$, where σ_V and σ_s are the minimum resolvable velocity and particle displacement, respectively ($\sigma_V = M\sigma_s/\tau$, where M is the spatial pixel resolution and τ is the pulse separation time). The minimum resolvable displacement σ_s is determined by the overall displacement error comprising both random and bias error, i.e. $\sigma_s = \lim_{s\to 0}(\Delta s)$, where $\Delta s = \sqrt{\epsilon_s^2 + \beta_s^2}$. It is assumed that the errors are evaluated at near zero displacement when using multi-pass correlation.

Various techniques have been developed to extend the dynamic range by increasing the maximum or reducing the minimum measurable displacement. For single-pass correlation algorithms, Keane and Adrian [6, 7] proposed the quarter window rule ($s_{max} < \frac{1}{4}d_I$) to avoid excessive loss of correlation strength due to in-plane displacement, yielding $DR_V^{(SP)} = \frac{1}{4}d_I/\sigma_s^{(SP)}$. The dependence of $\sigma_s^{(SP)}$ on a large number of parameters (e.g., particle image displacement, density and diameter, interrogation window size, image noise, digitisation and quantisation, velocity gradients) has been reviewed extensively for single-pass correlation [13, 22-24].

Using iterative window deformation with progressive grid refinement (multi-grid correlation), a tenfold reduction in uncertainty is achieved compared to single-pass correlation, with $\sigma_s^{(MG)} \cong 0.001$ pixel based on an analysis of Monte Carlo simulations of noiseless artificial particle images [15-17]. Multi-grid techniques partly decouple the maximum displacement and final interrogation window size, since the quarter rule [13] only applies to the first, coarse grid and not to subsequent passes. With an initial interrogation window size $k_g d_I$ and

a final size d_I (where typically k_g = 2-4), the dynamic range becomes $DR_V^{(MP)} = \frac{1}{4} k_g d_I / \sigma_s^{(MP)}$.

However, in realistic laboratory conditions, image noise and velocity gradients yield much larger uncertainty values than in artificial images, with typical values of $\sigma_s^{(MG)}$ around 0.1 pixel. Despite the use of advanced evaluation algorithms [19], a more realistic dynamic velocity range for multi-grid PIV is of the order of $DR_V \cong 160{:}1$ (for $k_g = 4$, $d_I = 16$ pixel).

By increasing the local pulse separation time, some studies have been able to achieve an improved dynamic range over conventional multi-grid PIV. Hain and Kähler [4] proposed an iterative, time-resolved multi-frame technique to compensate for the loss in dynamic range of CMOS sensors used in high speed PIV systems. This method selects at each location a pair of images within the sequence such that the particle image displacement is maintained approximately uniform (e.g. 10 pixels). In this case, the choice of optimal time separation is crucial. Multi-frame (MF) PIV has achieved good results compared to conventional PIV in low speed flows with a wide velocity range [3,4,10]. However, since MF PIV is proposed as an *alternative* to multi-grid PIV algorithms, it is difficult to benefit from advances in this field.

Some techniques increase the dynamic velocity range by combining information obtained at different pulse separation times [11, 12]. The multi-pulse separation (MPS) technique applies a greater pulse separation in regions of the flow field where the displacement magnitude would otherwise be of the order of the minimum resolvable displacement σ_s. This is analogous to high dynamic range (HDR) photography, which generates a composite image based on the weighted sum of a set of images taken at different exposure times [1, 8, 14]. Unlike linear superposition used in HDR photography, the MPS PIV algorithm determines a local optimum pulse separation by a criterion balancing correlation strength and measurement uncertainty. The reconstruction is nonlinear to avoid the propagation of spurious vectors resulting from the evaluation of images taken at an excessive pulse separation [11].

Using a constant value for the estimated displacement uncertainty (σ_s = 0.1 pixel), a significant improvement in the phase-averaged mean flow and turbulence intensity in an impinging synthetic jet flow was observed by [12] compared to conventional PIV. However, to extend the technique to time-resolved flows, a method for determining the local uncertainty was needed, as will be described further in this paper.

1.2 PIV Uncertainty Estimation

In order to implement advanced PIV techniques, different methods for estimating the local uncertainty $\Delta s = \sqrt{\epsilon_s^2 + \beta_s^2}$ have been evaluated. Previous estimates could only provide guidance on the expected error for an average measurement under specific image quality and flow conditions, but recent advancements have been made in the field of PIV uncertainty. Wilson and Smith [25] compared PIV velocity fields to the known particle displacement for a rectangular jet flow. For a specific combination of four parameters (displacement, shear, particle image density and particle image diameter), the four-dimensional uncertainty response was determined, termed the "uncertainty surface". Flow gradients, large particle images and insufficient particle image displacements resulted in elevated measurements of turbulence levels.

Charonko and Vlachos [2] developed a method for measuring error bounds to within a given confidence interval for a specific, individual measurement. The authors found that a strong correlation exists between the observed error and the correlation peak ratio Q (i.e., the ratio of the height of the first peak to the second in the spatial correlation domain). This correlation was found to hold regardless of flow condition and image quality.

Xue *et al.* [26] posited that the signal-to-noise-ratio (SNR) metrics calculated from the PIV correlation plane can be used to quantify the quality of correlation, and subsequently the uncertainty of an individual measurement. The relationship between SNR and uncertainty was explored for both the robust phase correlation (RPC) and standard cross correlation (SCC) processing. In the correlation metric, the uncertainty was a function of three terms: A Gaussian function used to account for uncertainty due to invalid measurements, a power-law term that describes the contribution of valid vectors to uncertainty, and a constant expressing the minimum achievable uncertainty.

1.3 Objectives

In this paper, the multiple pulse separation (MPS) PIV technique is extended towards time-resolved flows, using an axisymmetric unconfined turbulent jet flow as benchmark case and hot wire anemometry as reference

velocity measurement. Compared to earlier studies for non-time-resolved PIV [11, 12] a new criterion for the local optimal pulse separation has been developed and tested based on the estimated local displacement uncertainty as a modified signal-to-noise ratio.

2. Methodology: MPS PIV with local uncertainty estimation

2.1 Image acquisition

Persoons and O'Donovan [11] proposed the multiple pulse separation (MPS) technique to achieve high dynamic range (HDR) PIV results. Whereas multi-frame techniques [3, 4, 10] acquire single-frame image sequences $\{\dots, t, t+\delta t, t+2\delta t, \dots\}$, MPS PIV uses a customised timing system to acquire double-frame images $\{\dots, [t, t+k_{\tau,1}\tau_{min}], [t+\delta t, t+\delta t+k_{\tau,2}\tau_{min}], \dots\}$ with successive different pulse separation values $k_{\tau,i}\tau_{min}$ $(1 \le i \le N_\tau)$ at a given frame rate $1/\delta t$. Each image pair $[I(t), I(t+\tau_i)]$ with pulse separation $\tau_i = k_{\tau,i}\tau_{min}$ is correlated using conventional multi-grid algorithms resulting in the displacement fields $\vec{s}_i = \vec{s}(x, y, t, \tau_i)$.

In its simplest implementation using a conventional timing system, two pulse separation values can be included in the MPS algorithm by combining the information from $[I(t), I(t+\tau_{min})]$ (as double-frame cross-correlation) and $[I(t), I(t+\delta t)]$ (as time-series cross-correlation), where $\tau_1 = \tau_{min}$ and $\tau_2 = \tau_{max} = \delta t$ (and $N_\tau = 2$). This simple approach is used in this paper.

2.2 Optimum pulse separation criterion

To determine the optimum pulse separation $\tau_{opt}(x, y)$ for each location in a time- or phase-averaged flow, Persoons and O'Donovan [11] maximized the time-averaged product of the correlation peak ratio Q and a measure of the local vector quality, thereby balancing correlation strength and precision:

$$Q'(x, y, \tau) = \overline{Q(x, y, t, \tau)\left(1 - \frac{\sigma_s}{s_{mag}(x,y,t,\tau)}\right)} \tag{1}$$

where the displacement magnitude $s_{mag} = \tau\sqrt{U^2 + V^2}/M$. At each location (x, y), the maximum of $Q'(x, y, \tau_i)$ determines the local optimum pulse separation. This method assumed a constant minimal resolvable displacement value $\sigma_s(\approx \Delta s) = 0.1$ px. This order of magnitude seemed appropriate for multi-grid algorithms in realistic conditions, based on validation results in the review of Stanislas *et al*. [19].

However, assuming a constant displacement uncertainty is not a valid approach for time-resolved PIV, wherein Δs can vary significantly with respect to location and time. To overcome this limitation, the current study adopts a more general approach, defining the modified signal-to-noise ratio $G(\tau)$ as:

$$G(x, y, t, \tau) = Q(x, y, t, \tau)\left(\frac{s_{mag}(x,y,t,\tau)}{\Delta s(x,y,t,\tau)}\right)^m \tag{2}$$

The optimal pulse separation $\tau_{opt}(x, y, t)$, based on the local maximum of vector quality, is given by $\max_\tau[G(\tau)]$. This criterion does not assume constant pixel displacement, and as such is applicable to time-resolved data. Calculation of G is based on readily available correlation peak ratio, displacement magnitude but also requires determining the local uncertainty $\Delta s(x, y, t, \tau)$, which is described below. In this paper, an exponent $m = 4$ is chosen in Eq. (2). Values in the range $1 \le m \le 10$ shift the balance between correlation strength (low pulse separation) and signal-to-noise ratio (higher pulse separation).

2.3 Estimating the local displacement uncertainty and magnitude

Performing a Reynolds decomposition on the PIV displacement field $s(x, y, t)$ yields:

$$s(x, y, t) = \bar{s}(x, y) + s'(x, y, t) + \epsilon_s(x, y, t) + \beta_s(x, y, t) \tag{3}$$

where $\bar{s}(x, y)$ is the true time-averaged velocity and $s'(x, y, t)$ is the true turbulent velocity fluctuation, $\epsilon_s(x, y, t)$ is the random error and $\beta_s(x, y, t)$ is the bias error. Previous studies have used indirectly estimated error levels through mapping this relationship [20, 25], through quantifying the effect of errors on correlation space metrics [26] or by using high-resolution image analysis [18]. The current study adopts a heuristic approach, calculating an estimate for $\Delta s = \sqrt{\epsilon_s^2 + \beta_s^2}$ as the rms deviation from the local displacement

magnitude in a kernel of (n_x, n_y, n_t) adjacent vector grid locations in the spatiotemporal domain $[x, y, t]$, as shown in Fig. 1.

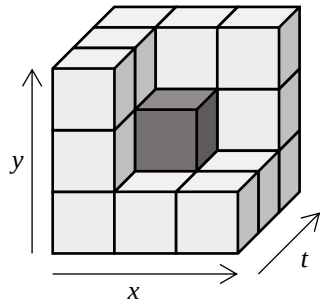

Fig. 1 Local uncertainty estimation based on the RMS deviation from the local displacement magnitude in a kernel of size (n_x, n_y, n_t) adjacent vector grid locations in the spatiotemporal domain $[x, y, t]$.

The local magnitude is defined as the mean value of the kernel, $s_{mag}(x,y,t) = \frac{1}{n_x n_y n_t}\sum s(x,y,t)$. Instead of the more computationally efficient mean value, the median could be used to ignore outliers. The local uncertainty estimate is defined as:

$$\Delta s(x,y,t) = \sqrt{\frac{1}{n_x n_y n_t}\sum\left[s(x,y,t) - s_{mag}(x,y,t)\right]^2} \quad (4)$$

Here, $n_x = n_y = 5$ and $n_t = 9$ (i.e., 225 elements), selected symmetrically around each vector grid location.

Referring to Eq. (3), the expression in Eq. (4) returns a combination of physical turbulent fluctuations and measurement uncertainty (both random and bias error contributions). Only if the turbulent fluctuation s' can be considered invariable over τ_i and the bias error β_s assumed small, will Eq. (4) accurately estimate the random error ϵ_s.The bias error is a function of the fill ratio of the camera, the PIV algorithm used and the degree of pixel locking due to sub-pixel sized tracer particles. Previous work has helped to quantify and minimize this error [5-7, 9, 21].

Although the uncertainty from Eq. (4) is contaminated by turbulent fluctuations and bias error, this should be of minor importance for the MPS algorithm. To determine the local optimal pulse separation, the values of $G(x,y,t,\tau_i)$ using Eq. (2) are compared *relative to each other* for all τ_i acquired in the *same flow field* with the *same optical arrangement and seeding conditions*.

By selecting a greater pulse separation ($\tau_{opt} \geq \tau_{min}$) in the low velocity region and a smaller pulse separation in the high velocity region, the minimum measurable velocity $\sigma_V \propto \sigma_s/\tau_{opt}$ and the dynamic range increases by a factor $k_\tau = \tau_{opt}/\tau_{min}$ compared to conventional multi-grid PIV:

$$DR_V^{(MPS)} = \frac{\frac{1}{4}k_g d_I/\tau_{min}}{\sigma_s^{(MG)}/\tau_{opt}} = k_\tau k_g \frac{\frac{1}{4}d_I}{\sigma_s^{(MG)}} = k_\tau DR_V^{(MG)} \quad (5)$$

In a practical experiment, the smallest pulse separation τ_{min} is chosen to limit the loss of correlation in regions of high velocity magnitude and shear, while the greatest pulse separation is chosen to give a measureable displacement magnitude in low velocity regions.

3. Experimental approach

3.1 Experimental apparatus

As a benchmark case, an axisymmetric turbulent air jet is selected, issuing from a settling chamber with 75mm internal diameter and flow straightener via a contoured nozzle with a radius of curvature of 10 mm and an exit diameter D = 5.0 mm, as depicted schematically in Fig. 2. Air is supplied from the building compressed air supply via an expansion valve and digital air mass flow meter (Alicat Scientific, Inc., 500 standard liters per minute, ±0.5% combined repeatability and accuracy). All experiments in the current paper are performed at Re = 9,100 (mean jet nozzle velocity $U_{jet} \cong 27$ m/s). Glycol-water based aerosol seeding is introduced partly

via a venturi in the air supply line and partly in the surrounding ambient air. The generated seeding droplets have a mean diameter between 0.2 and 0.3 μm and the particle images are 2 pixels in diameter. A high-repetition rate pulsed laser (Quantronix DarwinDuo double-pulsed Nd:YLF laser, 527nm, 15mJ at 2 kHz, 120ns pulse width) and a Photron Fastcam SA1 CMOS high-speed camera (1024^2 px, 5.4 kHz, 12 bit) are used for these experiments. A customized pulse timing system is available to apply different pulse separation values in successive pairs of frames, although for the experiments discussed in this paper, the simpler time-resolved double-frame approach is used as described in Section 2.1. The laser sheet is adjusted to 0.5 mm thickness, coplanar with the jet centerline. The optical scaling factor $M = 33$ μm/pixel.

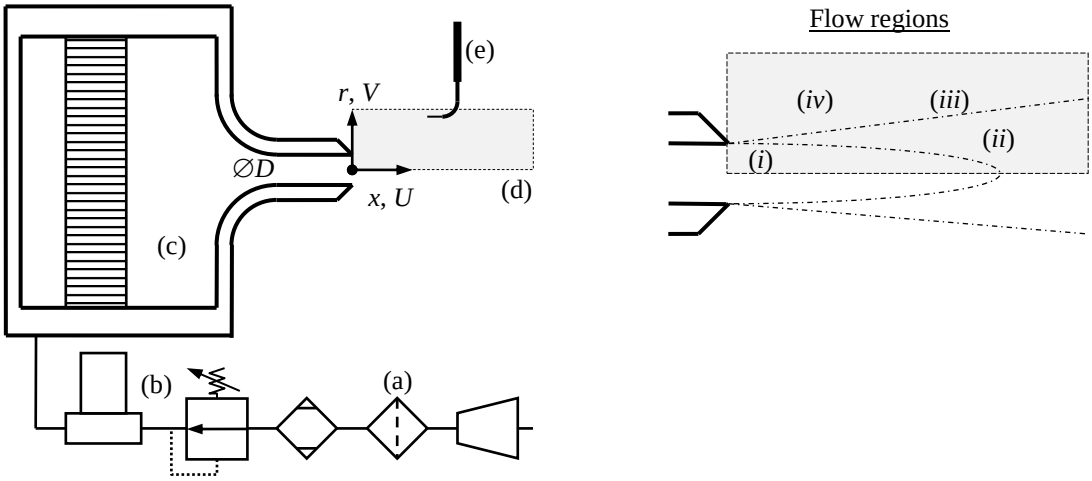

Fig. 2 Description of axisymmetric jet flow ((*i*) jet core, (*ii*) shear layer, (*iii*) outer shear layer, (*iv*) entrainment region): (a) compressor, filter and dryer, (b) pressure regulator valve and digital air flow meter, (c) settling chamber with flow conditioning and contoured nozzle, (d) PIV measurement region shown in Figs. 3-8, (e) hot-wire probe.

As an independent velocity measurement, a single component right-angle hot wire probe (Dantec Dynamics 55P14, 1.25 mm long, 5 μm diameter platinum-plated tungsten) is used with a constant temperature anemometer (Dantec Dynamics 54T30 MiniCTA) in selected characteristic locations in the flow field. The HWA measurements are performed after the PIV measurements, without seeding particles but otherwise identical flow conditions. The probe is positioned in the PIV measurement plane using the camera to check its actual position, with the wire aligned perpendicular to the PIV plane (represented by (e) in Fig. 2). In each point, data is acquired for several seconds at 20 kHz. The hot wire was calibrated in the same jet flow using the mass flow meter as reference. King's law was least-square fitted to describe the voltage-velocity relationship in the range 5-48m/s ($R^2 > 0.99$, rms deviation 2.8%).

3.2 PIV acquisition and vector evaluation

Double-frame images are acquired at 2920 Hz for 0.935 s corresponding to the maximum in-camera storage capacity. The pulse separation is set to $\tau_{min} = 10$ μs resulting in about 8 pixel displacement in the jet core region. This proved to be the maximum pulse separation without causing excessive loss of vectors in the shear layer as a result of the strong velocity gradient. Using the approach described in Section 2.1, the HDR algorithm is applied with $\tau_{min} = 10\mu s$ and $\tau_{max} = 1/(2920\text{Hz}) \cong 340\mu s$. Therefore, the maximum enhancement of the dynamic velocity range is 34:1.

Vector evaluation is performed with Lavision DaVis 7.2.2, using a multi-grid cross-correlation algorithm with initial interrogation window size of 64^2 px (2 passes, 75% overlap) and final interrogation window size of 32^2 px (2 passes, 50% overlap) with Whittaker reconstruction applied in the final pass. The vector evaluation is verified with in-house developed code in Trinity College Dublin, using higher order peak detection methods. HDR reconstruction is performed in a post-processing step on the resulting vector fields, using in-house developed Matlab code implementing the equations described in Section 2.

4. Experimental results

The results presented in this paper are determined for the same axisymmetric unconfined air jet at *Re* = 9,100

(D = 5 mm, mean jet nozzle velocity $U_{jet} \cong 27$ m/s). After verifying the symmetry of the flow field, only half plane flow fields are shown in this section ($0 \leq r/D \leq 2$ and $0 \leq x/D \leq 6$) for the sake of clarity.

4.1 Effect of HDR PIV on the time-averaged results

Figures 3 and 4 compare the PIV flow field measurements using conventional double-frame correlation for $\tau_{min} = 10$ μs (a, d); conventional time-series correlation for $\tau_{max} = 340$ μs (b, e); and the HDR PIV resulting from the combination of the above (c, f). All results shown in Figs. 3 and 4 are averaged over the maximum measurement duration of 0.935 s.

Figure 3(a-c) shows only a minor effect of using HDR PIV on the mean velocity magnitude, with a slightly smoother velocity contour line (at 0.02) in the entrainment region. However, Fig. 3(d-f) shows a significant reduction in measured turbulence intensity in the outer shear layer and entrainment region. The original conventional PIV results at $\tau_{min} = 10$ μs (Fig. 3d) exhibit a strong overestimation of turbulence intensity due to noisy low velocity vectors evaluated at the lower limit of the dynamic velocity range. The time-series PIV results for $\tau_{max} = 340$ μs (Fig. 3e) show more realistic low turbulence intensity in the entrainment region (0.2%-0.5%) yet fail to produce vectors in the central higher velocity region. The HDR turbulence field (Fig. 3f) seems to successfully combine the useful information from both vector evaluations into a wider dynamic range flow field.

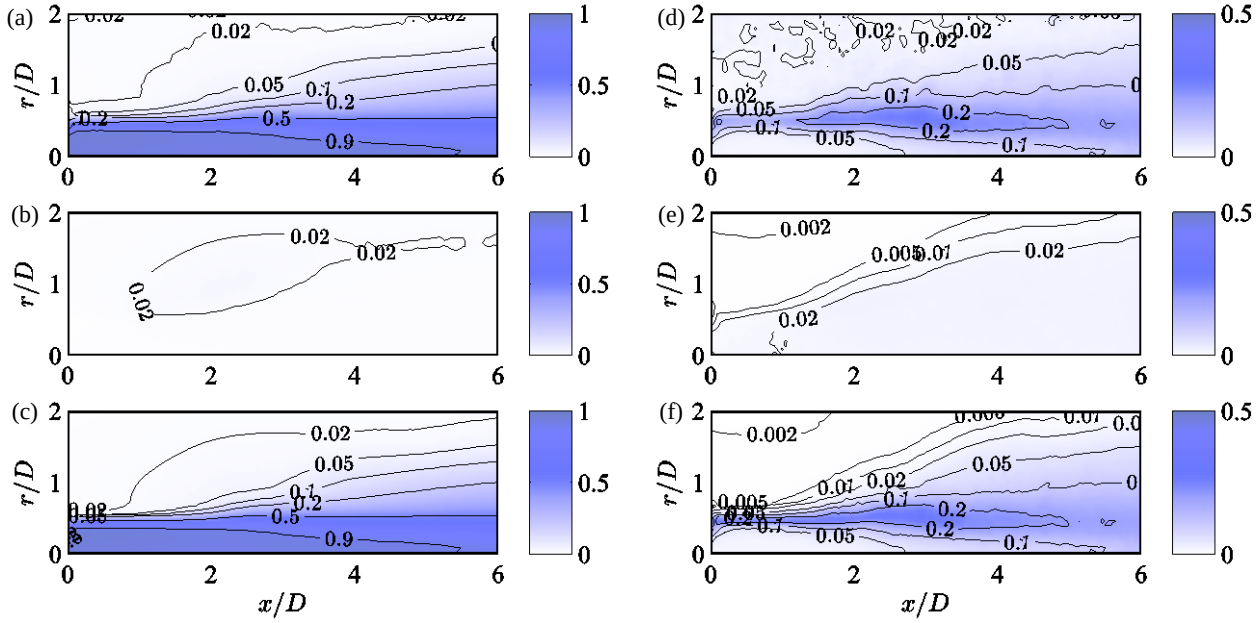

Fig. 3 Time-averaged (a-c) normalized velocity magnitude $\overline{\sqrt{U^2 + V^2}}/U_{jet}$ and (d-f) turbulent fluctuation magnitude $\sqrt{u'^2 + v'^2}/U_{jet}$ for an axisymmetric turbulent jet, using conventional PIV at pulse separation (a, d) $\tau = \tau_{min}$, (b, e) $\tau = \tau_{max}$ and (c, f) HDR PIV at $\tau_{opt}(x, y, t)$.

Figure 4(a-c) shows the time-averaged pulse separation (normalized by τ_{min}) used in the results shown in Fig. 3. For the HDR results, a gradual transition is observed from 1 in the central high velocity region to $\tau_{max}/\tau_{min} \cong 34$ beyond the outer shear layer. For each vector in time and space, either the lowest or highest pulse separation vector is selected. Since the time-averaged transition is gradual with a range of intermediate values in the shear layer, the HDR algorithm does not always select the same pulse separation for a given location. Instead, it adapts to the local instantaneous conditions determined by the value of $G = Q\left(\Delta s/s_{mag}\right)^{-m}$ (Eq. (2)), with the estimated uncertainty Δs calculated for each vector from Eq. (4).

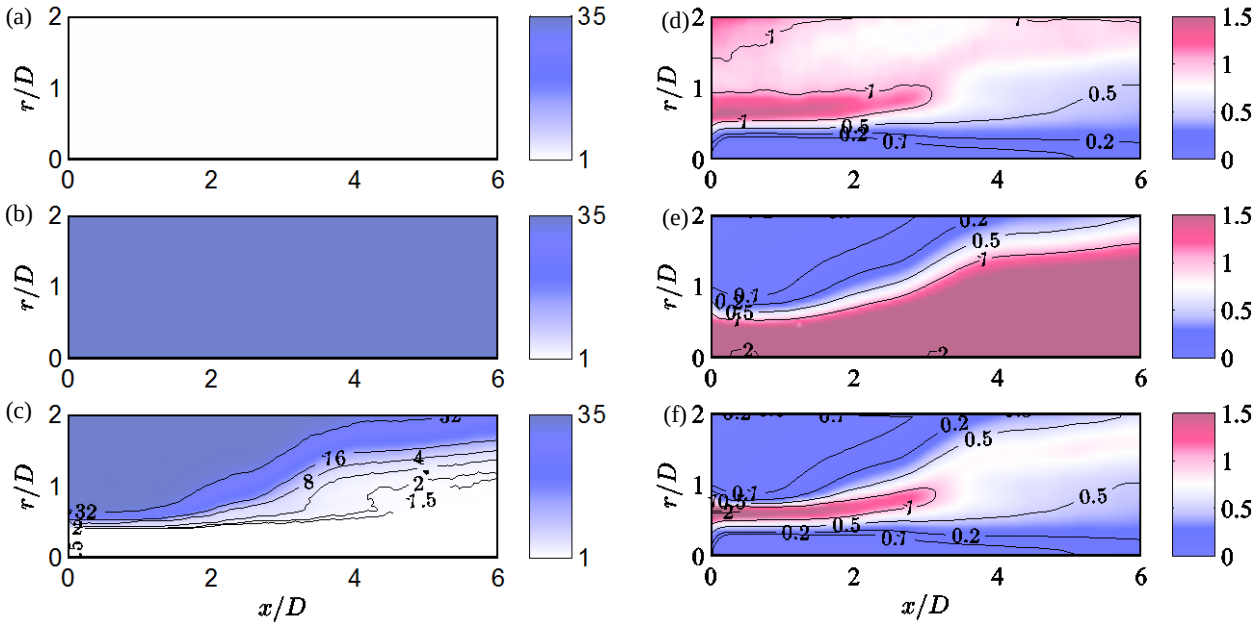

Fig. 4 Time-averaged (a-c) normalized pulse separation $\overline{\tau(x,y,t)/\tau_{min}}$ and (d-f) relative uncertainty $\overline{\Delta s/s_{mag}}$ using conventional PIV at pulse separation (a, d) $\tau = \tau_{min}$, (b, e) $\tau = \tau_{max}$ and (c, f) HDR PIV at $\tau = \tau_{opt}(x,y,t)$.

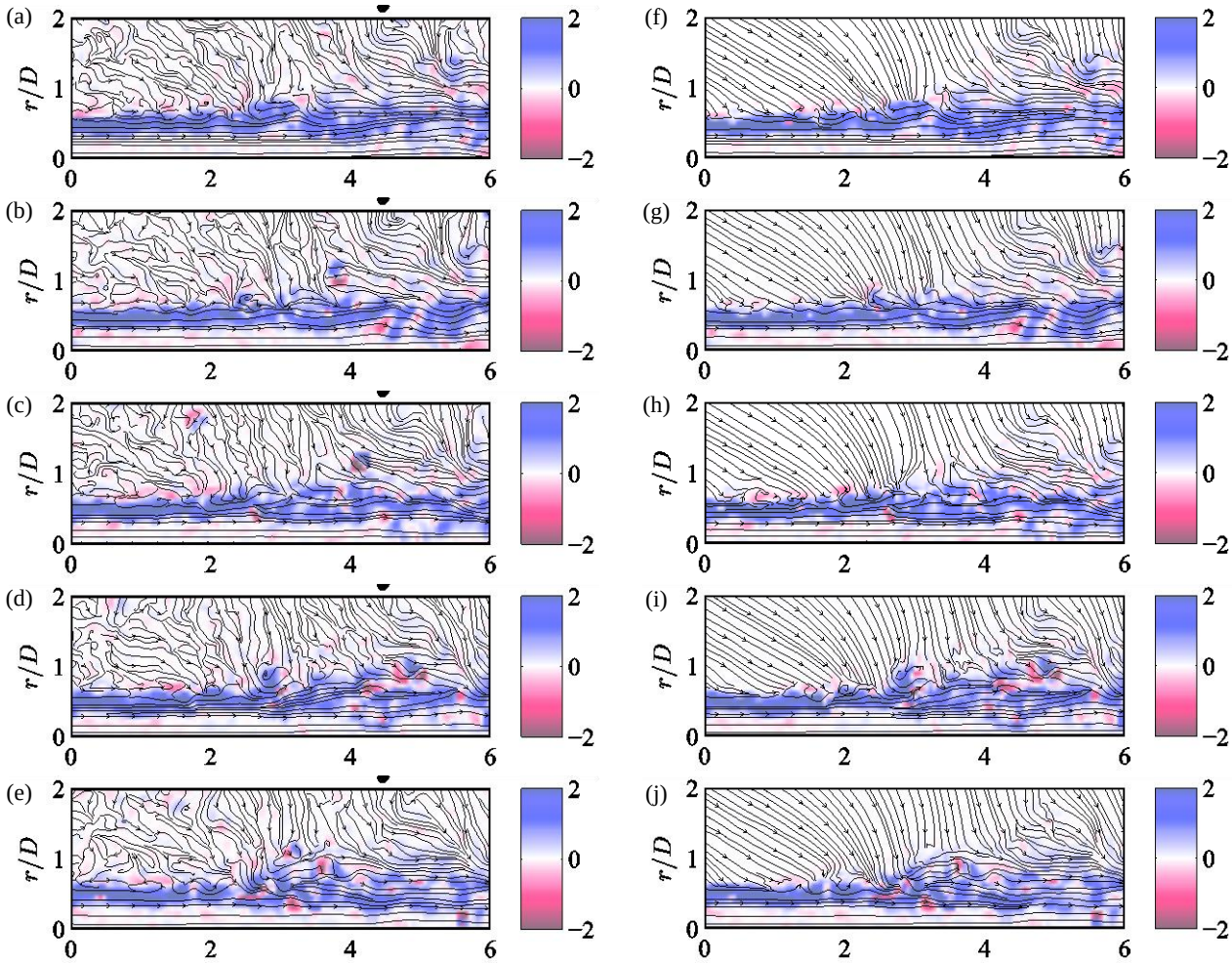

Fig. 5 Time-resolved sequence (top to bottom) of streamlines and normalized vorticity distribution $\omega(x,y,t)D/U_{jet}$ from (a,f) $t = t_0$ to (e,j) $t = t_0 + 4\delta t$ where $\delta t = 0.3425$ ms: (a-e) conventional PIV with pulse separation τ_{min} and (f-j) MPS PIV with local optimal pulse separation $\tau_{opt}(x,y,t)$

Figure 4(d-f) shows the time-averaged normalized uncertainty $\overline{\Delta s(x,y,t)/s_{mag}(x,y,t)}$, which takes quite high values in the entrainment region and outer shear layer near the nozzle for conventional PIV (Fig. 4d). This is relevant information since $\Delta s/s_{mag}$ is the inverse of a signal-to-noise ratio which appears directly in the vector quality metric $G = Q\left(s_{mag}/\Delta s\right)^m$ (Eq. (2)), along with the correlation peak ratio Q. The averaged relative uncertainty is much smaller in the same region for $\tau = \tau_{max}$ (Fig. 4e). For the HDR results (Fig. 4f) with $\tau = \tau_{opt}(x,y,t)$, the overall signal-to-noise ratio is higher. The most difficult region, also for HDR PIV, remains the shear layer near the orifice with its strong velocity gradients.

4.2 Effect of HDR PIV on the time-resolved results

Figure 5 shows a time sequence of the vorticity field using conventional PIV ($\tau = \tau_{min}$) on the left hand side, and HDR PIV on the right hand side for the same time records $t_0 + [0, \delta t, 2\delta t, 3\delta t, 4\delta t]$, where t_0 is an arbitrarily chosen time within the measurement duration. Instantaneous streamlines are superimposed to highlight the difficulty experienced by conventional PIV in the entrainment region, due to the low velocity magnitude there. The HDR results in Fig. 5(f-j) show a seamless transition from smooth streamlines (resulting mainly from the highest pulse separation vectors) to high velocity turbulent jet flow (resulting from the small pulse separation vectors), at each instant in time.

Figures 6-8 show time and frequency domain plots of the measured velocity in 3 characteristic locations, where hot-wire anemometry measurement were also taken in the same flow field without seeding. Each location is indicated by the cross marker in the flow field in Figs. 6-8(a). The locations were chosen (a) in the middle of the jet core region, (b) in the far shear layer, and (c) in the entrainment region. The locations used in Figs. 6-8 correspond to the exact location of the hot wire probe as determined in the camera image.

The hot wire anemometry (HWA) readings were acquired at 20 kHz while the PIV recording was done at 2.92 kHz, hence the difference in the frequency domain range for the signals. In Fig. 6, the HWA velocity shows evidence of harmonic oscillations of the same order of magnitude as the natural vortex shedding frequency of the jet. Because the PIV recording rate is lower than the shedding frequency for this jet flow, the same oscillations are not picked up in the PIV results.

In terms of the comparison between conventional and HDR PIV results, Fig. 6 ($[x,r] \cong [3.0,0.1]D$) shows that the HDR results rightly completely overlap the results for $\tau = \tau_{min}$ since no valid vectors were determined at the high pulse separation in the jet core region. A similar situation is observed in Fig. 7 in the far shear layer ($[x,r] \cong [4.5,0.8]D$). Figure 8 shows the HDR algorithm giving preference to the high pulse separation results in the entrainment region ($[x,r] \cong [1.5,1.1]D$) since the signal-to-noise ratio is enhanced in this low mean velocity region.

Figure 9 compares the PIV results in a location in the outer shear layer ($[x,r] \cong [3.0,1.1]D$) where unfortunately no HWA measurements were taken at the time of the experiments. In this location, the time trace shows the HDR PIV velocity switching between the low and high pulse separation data, maximizing the vector quality for each time record.

5. Conclusions

In this paper, the multiple pulse separation (MPS) technique for high dynamic range (HDR) PIV has successfully been extended towards *time-resolved* measurements. As a benchmark case, a high-repetition rate pulsed laser and camera system are used in combination with an axisymmetric turbulent air jet flow at *Re* = 9,100 (*D* = 5 mm).

In order to implement the time-resolved HDR PIV technique, the method developed previously for non-time-resolved PIV [11, 12] has been modified into a new criterion for the local optimal pulse separation. This criterion is based on a new vector quality metric G (see Eq. (2)) comprising the correlation peak ratio Q and the estimated local displacement uncertainty as a signal-to-noise ratio $s_{mag}/\Delta s$.

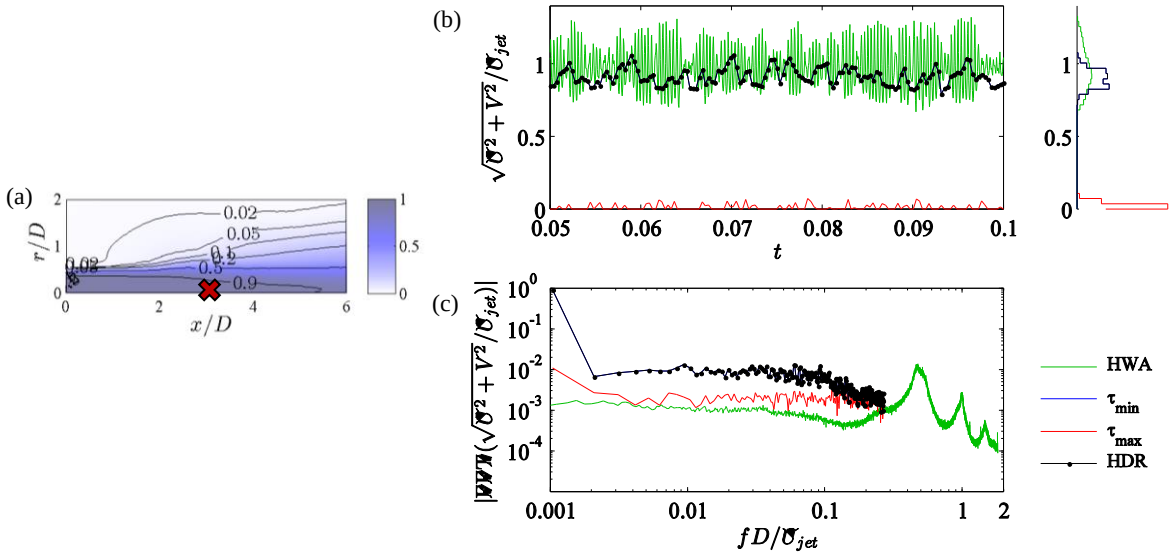

Fig. 6 Normalized velocity magnitude $\sqrt{U^2+V^2}/U_{jet}$ at location $[x,r] \cong [3.0,0.1]D$ (represented by the × marker in (a)) in (b) time domain and (c) FFT frequency domain: (—) hot-wire anemometer, (—) conventional PIV at pulse separation $\tau = \tau_{min}$, (—) $\tau = \tau_{max}$ and (–•–) HDR PIV at $\tau = \tau_{opt}(x,y,t)$.

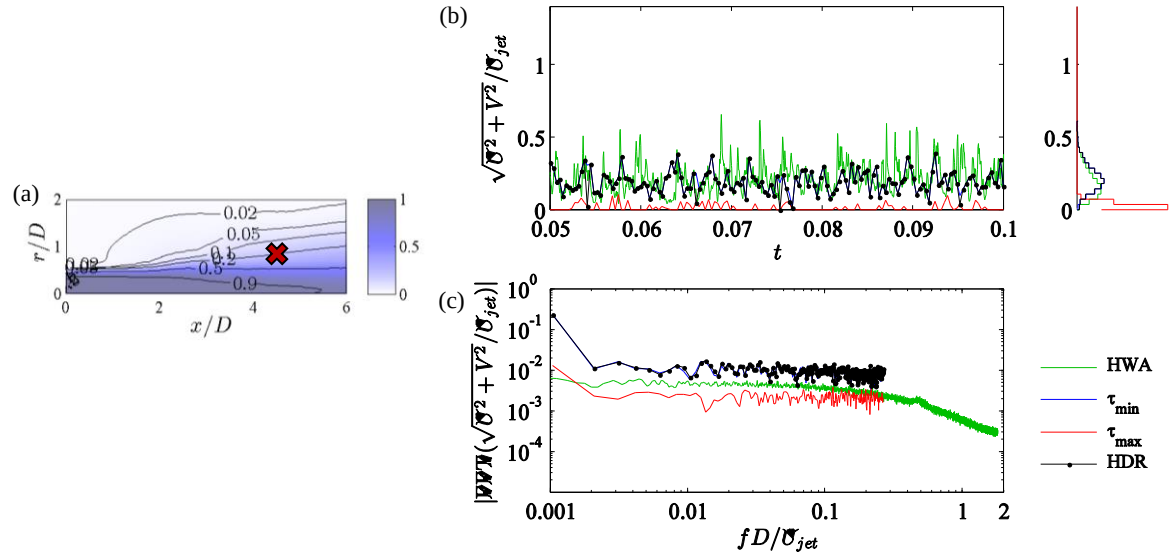

Fig. 7 Normalized velocity magnitude $\sqrt{U^2+V^2}/U_{jet}$ at location $[x,r] \cong [4.5,0.8]D$ (represented by the × marker in (a)) in (b) time domain and (c) FFT frequency domain: (—) hot-wire anemometer, (—) conventional PIV at pulse separation $\tau = \tau_{min}$, (—) $\tau = \tau_{max}$ and (–•–) HDR PIV at $\tau = \tau_{opt}(x,y,t)$.

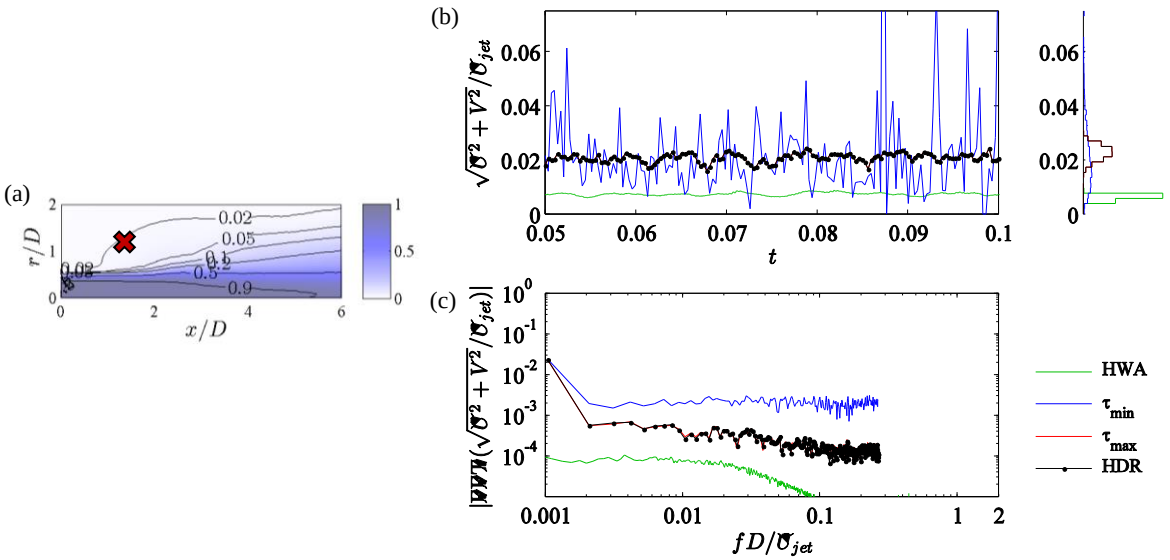

Fig. 8 Normalized velocity magnitude $\sqrt{U^2+V^2}/U_{jet}$ at location $[x,r] \cong [1.5,1.1]D$ (represented by the × marker in (a)) in (b) time domain and (c) FFT frequency domain: (—) hot-wire anemometer, (—) conventional PIV at pulse separation $\tau = \tau_{min}$, (—) $\tau = \tau_{max}$ and (–•–) HDR PIV at $\tau = \tau_{opt}(x,y,t)$.

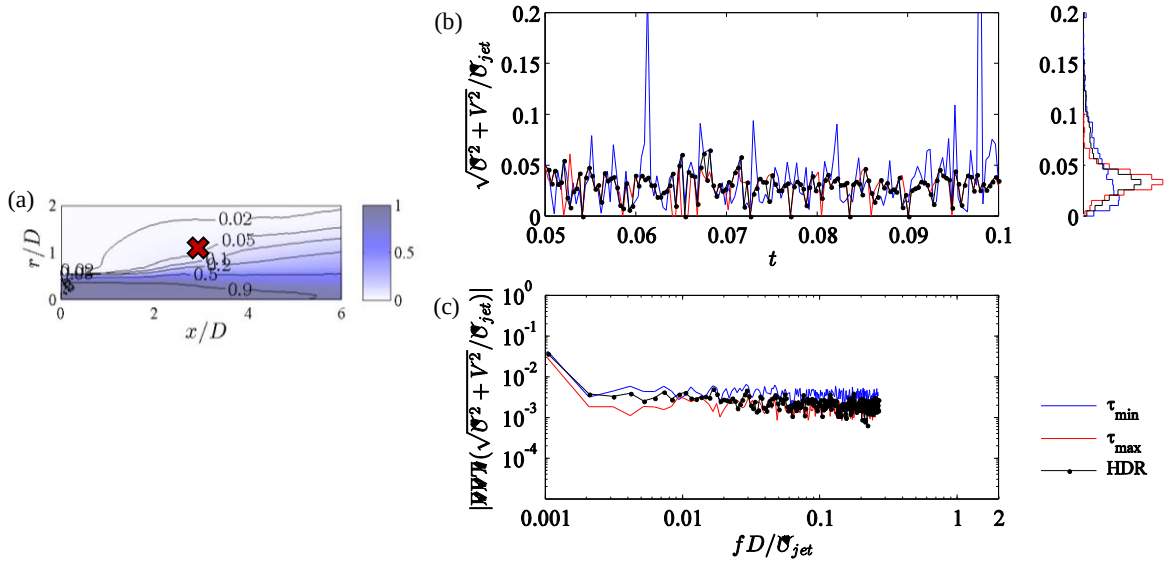

Fig. 9 Normalized velocity magnitude $\sqrt{U^2+V^2}/U_{jet}$ at location $[x,r] = [3.0,1.1]D$ (represented by the × marker in (a)) in (b) time domain and (c) FFT frequency domain: (—) conventional PIV at pulse separation $\tau = \tau_{min}$, (—) $\tau = \tau_{max}$ and (–•–) HDR PIV at $\tau = \tau_{opt}(x,y,t)$.

The HDR method automatically selects the most optimal local pulse separation and corresponding vector as a function of space and time, by maximizing the aforementioned vector quality metric $\max_{\tau}[G(\tau)]$. The user-defined parameters include (i) the size of the kernel in Eq. (4) and (ii) the exponent m in Eq. (2), which is set at $m = 4$ in this paper. Values between 1 and 10 shift the balance in the criterion between correlation strength Q and signal-to-noise ratio $s_{mag}/\Delta s$, however the criterion seems robust enough to avoid invalid vectors determined at excessive pulse separations. The chosen kernel size is $5 \times 5 \times 9$ ($n_x = n_y = 5$ and $n_t = 9$), which is a compromise between calculation time and the desired spatiotemporal resolution of the magnitude and rms deviation metrics.

The most significant improvement of using HDR PIV was observed in the turbulence intensity fields in the entrainment and outer shear layer regions. The dynamic velocity range in this flow field was increased by a factor 34:1 (1.5 orders of magnitude), from an approximate value of 160:1 for conventional PIV to 5,400:1.

The HDR PIV method is implemented entirely based on readily available data. It has a low computational cost and since it is implemented as a post-processing routine, it is fully compatible with all conventional multi-grid vector evaluation algorithms, such as those implemented in commercial PIV software packages.

References

1. Battiato S, Castorina A, Mancuso M (2003) High dynamic range imaging for digital still camera: An overview. J Electron Imaging 12:459-469.
2. Charonko JJ, Vlachos PP (2013) Estimation of uncertainty bounds for individual particle image velocimetry measurements from cross-correlation peak ratio. Meas Sci Technol 24:065301.
3. Fincham A, Delerce G (2000) Advanced optimization of correlation imaging velocimetry algorithms. Exp Fluids 29:S13-S22.
4. Hain R, Kähler CJ (2007) Fundamentals of multiframe particle image velocimetry (PIV). Exp Fluids 42:575-587.
5. Huang H, Dabiri D, Gharib M (1997) On errors of digital particle image velocimetry. Meas Sci Technol 8(12):1427.
6. Keane RD, Adrian RJ (1990) Optimization of particle image velocimeters. Part I: Double pulsed systems. Meas Sci Technol 1:1202-1215.
7. Keane RD, Adrian RJ (1992) Theory of cross-correlation analysis of PIV images. Appl Sci Res 49:191-215.
8. Mann S, Picard RW (1995) On being ‘undigital’ with digital cameras: Extending dynamic range by combining differently exposed pictures. In Proc IS&T Annu Conf Imaging on the Information Superhighway, Washington, DC, USA, pp. 442-448.
9. Nogueira J, et al. (2011) Quantitative evaluation of PIV peak locking through a multiple Δt strategy: relevance of the rms component. Exp Fluids 51:785-793.
10. Pereira F, Ciarravano A, Romano GP, Di Felice F (2004) Adaptive multi-frame PIV. In Proc 12th Int Symp on Applications of Laser Techniques to Fluid Mechanics, Lisbon, Portugal, 12-15 July, 2004
11. Persoons T, O’Donovan TS (2010) High dynamic velocity range particle image velocimetry using multiple pulse separation imaging. Sensors 11(1):1-18.
12. Persoons T, Farrelly R, McGuinn A, Murray DB (2010) High dynamic range whole-field turbulence measurements in impinging synthetic jets for heat transfer applications. In Proc 15th Int Symp on Applications of Laser Techniques to Fluid Mechanics, Lisbon, Portugal, 5-8 July, 2010.
13. Raffel M, Willert C, Kompenhans J (1998) Particle Image Velocimetry: A Practical Guide (Eds. Adrian RJ, et al.), Springer-Verlag, Berlin, Germany, pp 134-146.
14. Reinhard E, Ward G, Pattanaik S, Debevec P (2005) High Dynamic Range Imaging: Acquisition, Display, and Image-Based Lighting. Morgan Kaufmann Publishers Inc., San Francisco, CA, USA.
15. Scarano F(2002) Iterative image deformation methods in PIV. Meas Sci Technol 13: R1-R19.
16. Scarano F, Riethmuller ML (2000) Advances in iterative multigrid PIV image processing. Exp Fluids 29:S51-S60.
17. Scarano F, Riethmuller ML (1999) Iterative multigrid approach in PIV image processing using discrete window offset. Exp Fluids 26:513-523.
18. Sciacchitano A, Wieneke B, Scarano F (2013) PIV uncertainty quantification by image matching. Meas Sci Technol 24:045302.
19. Stanislas M, Okamoto K, Kähler CJ, Westerweel J (2005) Main results of the second international PIV challenge. Exp Fluids 39:170-191.
20. Timmins BH, Wilson BW, Smith BL, Vlachos PP (2012) A method for automatic estimation of instantaneous local uncertainty in particle image velocimetry measurements. Exp Fluids 53:1133-1147.
21. Wereley ST, Gui L, Meinhart CD (2002) Advanced algorithms for microscale particle image velocimetry. AIAA J 40:1047-1055.
22. Westerweel J (1997) Fundamentals of digital particle image velocimetry. Meas Sci Technol 8:1379-1392.
23. Westerweel J (2008) On velocity gradients in PIV interrogation. Exp Fluids 44:831-842.

24. Westerweel J, Dabiri D, Gharib M (1997) The effect of a discrete window offset on the accuracy of cross-correlation analysis of digital PIV recordings. Exp Fluids 23:20-28.
25. Wilson BM, Smith BL (2013) Uncertainty on PIV mean and fluctuating velocity due to bias and random errors. Meas Sci Technol 24:035302.
26. Xue Z, Charonko JJ, Vlachos PP (2014) Particle image velocimetry correlation signal-to-noise ratio metrics and measurement uncertainty quantification. (preprint arXiv:1405.3023)